1
2
3
4
5
6
7
8
9
10
11
12
13
14
15

A Feasibility Study of Radar-Based Shape and Reflectivity Reconstruction Using Variational Methods

Samuel Bignardi[1]‡**, Anthony Joseph Yezzi**[1]**, Alper Yildirim**[1]**,**
Christopher F. Barnes[1]**, Romeil Sandhu**[2]

[1]School of Electrical and Computer Engineering, Georgia Institute of Technology
[2]Department of Computer Science, Stony Brook University

E-mail: `sbignardi3@mail.gatech.edu`, `anthony.yezzi@ece.gatech.edu`
`alperyildirim@gatech.edu`, `romeil.sandhu@stonybrook.edu`,
`chris.barnes@gatech.edu`

Abstract. Remote sensing radar techniques provide highly detailed imaging. Nevertheless, radar images don't offer directly retrievable representations of shape within the scene. Therefore, shape reconstruction from radar typically relies on applying post-processing computer vision techniques, originally designed for optical images, to radar imaging products. Shape reconstruction directly from raw data would be desirable in many applications, e.g. in computer vision and robotics. In this perspective, inversion seems an attractive approach. Nevertheless, inversion has seldom been attempted in the radar context, as high frequency signals lead to energy functionals dominated by tightly packed narrow local minima. In this paper, we take the first step in developing a framework in which radar signals and images can be jointly used for shape reconstruction. In particular, we investigate the feasibility of shape reconstruction by inversion of pulse-compressed radar signals alone, collected at sparse locations. Motivated by geometric methods that have matured within the fields of image processing and computer vision, we pose the problem in a variational context obtaining a partial differential equation for the evolution of an initial shape toward the shape-reflectivity combination that best reproduces the data. While doing so, we highlight several non-obvious difficulties encountered and discuss how to surpass them. We illustrate the potential of this approach through three simulated examples and discuss several implementation choices, including boundary conditions, reflectivity estimation, and radiative models. The success of our simulations shows that this variational approach can naturally accommodate radar inversion and has the potential for further expansion toward active surfaces and level set applications, where we believe it will naturally complement current applications with optical images.

‡ The author to whom any correspondence should be addressed.

Radar-Based Reconstruction Using Variational Methods   2

1. Introduction

Inverse methods, where measured data are compared with simulated output from a model to recover the optimal values of the parameter set controlling the response of such model, have been widely applied in many disciplines (Groetsch 1984, Tarantola 2005). For example, geophysics (Loke & Barker 1996, Herman 2001, Park et al. 1999, Louie 2001), engineering and non destructive testing (Sambuelli et al. 2011, Cosentino et al. 2011), medicine (Hounsfield 1973, Bertero & Piana 2006, Comelli et al. 2020), computer vision (Hailin et al. 2002, Yezzi & Soatto 2003), and remote sensing (Deepak. 1977).

Inversion techniques have also been applied to tackle shape reconstruction. These include the variational approaches (commonly encountered in computer vision) which express the iterative optimisation in form of a partial differential equation (PDE); Active Surfaces and Level Set Methods being among the most popular. In the context of computer vision, active surfaces have been exploited both for the segmentation of data volumes (Yezzi et al. 1997, Cheng et al. 2009, Haukas et al. 2013, Shafiq et al. 2015, Comelli et al. 2020) and for the reconstruction of the three-dimensional shape of an object of interest using images acquired from sparse cameras (Yezzi & Soatto 2003, Hailin et al. 2002, Jin et al. 2003, Gallego et al. 2011). These methods rely on partitioning the 3D space by means of a surface which is iteratively evolved until it wraps around the object of interest. Typically, the task is posed as a classic local optimisation scheme, where the geometric surface is evolved in order to minimise an energy. While shape reconstruction from images finds several applications, e.g. in robotics and computer vision, optical approaches have many limitations. The inclusion of radar sensing within such inversion frameworks would be very desirable, as radar can easily be employed at night time and can probe a scene even when weather conditions would hinder optical alternatives. However, before visible/radar joint inversion can be tackled, it is necessary to investigate the feasibility of handling radar data within existing variational schemes. In particular, candidate adaptations of such inversion schemes should be sufficiently stable to allow shape reconstruction from radar data alone. **We devise an inversion approach to simultaneously reconstruct shape and reflectivity of a three-dimensional structure (scene) directly from measured radar data (i.e. high frequency back scattered electromagnetic signals), collected at sparse locations**. Our approach to the problem will blend concepts from different scientific domains. As such, before fully describing our contribution (section 1.3), we provide a brief introduction from the domains of radar remote sensing and waveform inversion.

Radar-Based Reconstruction Using Variational Methods   3

1.1. Radar Remote Sensing

Established radar imaging techniques leverage recording the reflected echo signal, most often a linear chirp signal (e.g figure 1a), back-scattered toward the emitting antenna. Echoes recorded at multiple locations, either by antenna arrays or by moving antennas are used to acquire multi-view information from which an image of the illuminated scene is formed. Historically the development of this technology was application-specific and implementation choices were dominated by hardware capabilities. A wide variety of approaches to the image formation exist nowadays (Curlander & McDonough 1991, Carrara et al. 1995, Soumekh 1999), and a thorough review is beyond the scope of this paper.

The Synthetic Aperture Radar (SAR), in all its flavours, might be considered a good example of this entire class of applications (Curlander & McDonough 1991, Carrara et al. 1995, Soumekh 1999). SAR leverages a moving antenna, emitting pulses at regular intervals to illuminate the scene from multiple viewpoints. Fundamental aspects of each data acquisition are the choice of working parameters related to the emitted signal, such as: frequency band, pulse duration; as well as geometric parameters, such as the number and locations where the signal is emitted/collected and antenna orientation, all of which rule the achievable resolution of the produced image. In Stripmap mode SAR (Munson, Jr 1987) for example, the antenna moves along a straight line and has a fixed orientation with respect to direction of the movement. In spotlight mode SAR, the antenna is moved instead along a linear or circular trajectory while the beam is steered to point the scene (Curlander & McDonough 1991, Carrara et al. 1995, Soumekh 1999). Concerning data processing, if we focus on just one of these approaches, the "holographic approach" (Farhat 1975), for example, we must emphasise that in order to translate the data from the aperture-range domain (i.e the antenna locations - distance to the scene), to the space-space domain (i.e. the image), signal processing techniques (typically, pulse compression and Stolt formatting), although involved, are sufficient to achieve the final result and no inversion is necessary. This consideration remains true for the most recent Volumetric SAR (VOLSAR) which exploits the holographic approach to produce a three dimensional reflectivity volume (Barnes & Prasad 2018). It is a common denominator of all radar-based approaches to search for ever higher resolutions of the produced image.

Ultimately, the key aspect of SAR processing is that, in order to form such an image and correctly achieve the maximum pixel-wise resolution, the information from the echoes at different antennas must be coherently summed (i.e. phases must be synchronised to the wavelength level). Such a careful handling of signal phases requires extremely precise control of the antenna collocation, which becomes a limitation as the frequency band of the emitted signal increases.

Shape reconstruction has been investigated in the radar imaging context as well. For example, (Das & Boerner 1978) proposed an approach based on the Radon transform showing that the challenge is equivalent to the problem of image reconstruction from projections. In this early approach radar signals were Fourier transformed to the

Radar-Based Reconstruction Using Variational Methods   4

frequency domain, and only a subset of frequencies were considered for the shape reconstruction. Gonzalez-Valdes et al. (2013) used an iterative algorithm coupled with a frequency hopping strategy to retrieve the shape of a two dimensional perfect electric conductor body from data collected at several transmitting–receiving antennas placed around it. Shape reconstruction finds application also for the determination of asteroids shape from delay-Doppler radar images (Hudson 1993, Brozovic et al. 2009). These methods are related to techniques in inverse SAR (Walker 1980). SAR interferometry (ifSAR) (Bamler & Hartl 1998) is routinely used to obtain land digital elevation models (DEM), or to monitor elevation changes over time from a reference DEM. This approach leverages phase difference between pairs of SAR images obtained from data collected either at slightly displaced trajectories or at different times. Three dimensional reconstruction is also tackled combining SAR and polarimetry (Cloude 2010), as polarization effects experienced by electromagnetic waves when reflected by the scene carry a wealth of information about the 3D nature of the scene. With these approaches, 3D images (i.e. data volumes) can be successfully obtained (Hamasaki et al. 2005). Additional methodologies attempt extracting complex geometric features adopting stereo or stereogrammetry based strategies (Koyama et al. 2016, Bagheri et al. 2018).

Summarising, shape reconstruction in radar applications is mostly achieved starting from images. Formation of such images requires careful processing and a regular acquisition geometry of the synthetic aperture in order to achieve the necessary coherent summing. Only after image formation is the shape reconstruction challenge finally cast into an inversion framework. An interesting observation about shape reconstruction from SAR images is brought by Thomas et al. (1989). They leveraged active surfaces for reconstruction of land topography exploiting the difference in shading between multiple SAR images and pointed out that the geometry can only be recovered with much lower resolution when compared to the initial images. Indeed, SAR images typically possess a detailed pixel-level granular structure (speckle), which requires strong regularisation in order to make the energy functional sufficiently smooth for stereo reconstruction and local minimisation techniques. **The key lesson is that the level of detail needed to make radar images most useful for human visual inspection is unnecessary to reconstruct the general shape of a scene, and we could therefore conceptually avoid coherent summation. In turn, this means we could build our shape reconstruction on the inversion of individual echo signals, avoiding image formation entirely.**

1.2. Inversion of oscillating signals

Limited preliminary work (Bignardi et al. 2012, Cook et al. 2014, Yildirim & Yezzi 2018) has demonstrated that shape reconstruction directly from remotely sensed oscillating signals is feasible, provided that a proper energy functional is defined. To construct a well behaved radar-based energy functional we must first deal with the oscillatory nature of radar signals. In this sense, an interesting example is found in geophysics,

Radar-Based Reconstruction Using Variational Methods   5

in the context of Full Waveform Inversion (FWI). In FWI, seismic signals collected by an array of geophones are used in the framework of inversion to infer the P-waves velocity distribution in the subsurface (Virieux & Operto 2009, Raknes & Arntsen 2014). FWI tackles such a task by minimising the distance between measured and simulated seismograms (either expressed in time or frequency domain), leveraging a residual error function $\mathcal{E}$ posed in least squares form. Considering just one receiver:

$$\mathcal{E} = \left\langle \left(\mathbf{u} - \mathbf{u^0}\right), \left(\mathbf{u} - \mathbf{u^0}\right) \right\rangle = \int \left(\mathbf{u}(s) - \mathbf{u}^0(s)\right) \left(\mathbf{u}(s) - \mathbf{u}^0(s)\right)^* ds, \qquad (1)$$

where s is either time or frequency. To be successful, the local optimisation requires a smooth energy functional and the initial model must be already in the basin of attraction of the global minimum. Unfortunately, an energy defined as in equation (1), based on the difference of oscillating signals possesses a large number of local minima. A difficulty strictly related to this aspect is the commonly known "cycle skipping", effectively illustrated in figure 7 of Virieux & Operto (2009). This phenomenon is easily understood considering the frequency domain. While cycle skipping typically affects several frequencies simultaneously, let's consider just one as example. When the harmonic of the simulated signal nearly matches the corresponding harmonic in the data, but shifted by an integer number of periods, the energy minimisation will push the contribution of that frequency to the energy functional toward a local minimum and therefore, to a incorrect model. **It is important to note that cycle-skipping affects both the time and frequency domain; and becomes increasingly severe as frequency increases**. In the frequency range typically investigated by FWI (i.e. $<$ $100 \, Hz$), the initial model already needs to be "very good" (typically a smooth version of the reality) for the inversion to succeed.

Since radar sensing leverages a much higher frequency range, managing cycle skipping is crucial to the feasibility of our application. Therefore, in the "Method" (section 2) we will illustrate such a phenomenon in the radar inversion context (figure 1a,b), and propose a strategy to tackle this issue.

1.3. Motivation and contribution of the present work

Optical devices provide information on two lateral dimensions (i.e. the two dimensions in an image). Radar conveys information on the range (i.e. depth), which is precisely the dimension that is lost in optical imaging. Therefore, combining optical and radar data would convey, in principle, complementary information that could be powerfully exploited within the context of a unified inversion framework. In our view, active surfaces and the level set method would provide the ideal environment, as they can naturally handle topological changes of the geometric model (i.e. the shape) being reconstructed. However, in order to explore the feasibility of using these mathematical frameworks with radar data, we first investigate the simplified case in which the surface of interest is parametrized in form of a graph of a function. While with this simplification the surface is not technically an active surface anymore, its evolution still belong within

the general family of variational methods and more importantly, conclusions can be easily generalised to Active Surfaces.

Developing a unified framework requires investigating the mathematical foundation to include radar information in the variational approach, and this task represents a stand-alone reconstruction problem.

In this paper, we leverage radar signals (i.e. high frequency back scattered electromagnetic signals) emitted and received by a set of sparse antennas to reconstruct shape and reflectivity of a three-dimensional structure. We develop a time domain approach to the reconstruction problem by leveraging time-domain signals after pulse compression. Methods motivated by a similar philosophy can also be formulated in the frequency domain, and we indeed develop such a strategy by leveraging stretch processing in a concurrent companion paper (Yildirim et al. 2020). This paper (and its companion paper) take a first step towards establishing a framework in which optical approaches and radar can naturally blend and where well established approaches from computer vision can be fully exploited.

In what follows we describe a general approach for embedding high-frequency signals in a local inversion mathematical framework. What we obtain, is a variational method from which a partial differential equation for the evolution of an initial shape toward the shape that best reproduces the radar data is obtained.

Therefore, differently from traditional radar approaches, which focus on image formation first, and differently from the computer vision domain where PDE methods on images are well established and do not pose any challenge, we tackle the reconstruction problem directly by inverting the signals back-reflected from the scene. Even with the graph surface simplification, we show that inclusion of such highly oscillating signals in variational methods and PDE poses several nontrivial challenges that must be carefully addressed before moving toward active surfaces, which will be a matter for future work. In the following, we illustrate both challenges and solutions by means of three examples possessing increasing level of sophistication. We emphasise that the graph surface is used only for mathematical convenience and not to tackle radar applications for which a well established approach already exists (e.g. land topography estimation). On the contrary, our interest is in 3D shape reconstruction as it is often encountered in robotics and computer vision applications. In examples 1 and 2, we use two different radiative assumptions and show how a piece-wise constant reflectivity can be estimated. While in these examples the shape to be reconstructed is relatively simple, in Example 3 we show how both shape and reflectivity can be retrieved even for a shape model possessing high curvature features and occluded visibility. In addition, example 3 will investigate the case of noisy simulated data.

2. Method

We consider a scene/object probed by a set of A sparse radar antennas or alternatively, by one antenna moving along an irregular trajectory and probing the object from A

locations. We assume that a linear frequency modulated (LFM) chirp pulse is emitted, and the corresponding echo is recorded at same location $\mathbf{x}_a$, where index a identifies a specific location. Recording locations, as well as the parameters characterising the emitted signal are assumed known. With this premises, we assume our data to comprise A time series, after pulse compression has been applied. In the following we will refer to these quantities as "raw signals" or "raw data". In our inversion scheme, we consider a model in which the back scattering object can be represented by a smooth surface $\mathcal{S}$ on which a smooth, complex reflectivity g (viz. a continuous distribution of point scatterers), is defined. Such surface is iteratively evolved in order to minimise the following general energy functional:

$$E\left(u(\mathcal{S}, G), u^0\right) = \mathcal{E}\left(u(\mathcal{S}, G), u^0\right) + \frac{\alpha_1}{2} R_\mathcal{S} + \frac{\alpha_2}{2} R_G \, , \tag{2}$$

where u^0 is an observable derived from the raw data and $u(\mathcal{S}, G)$ is the corresponding simulated signal, which depends on the surface $\mathcal{S}$ and through the quantity $G = gg^*$, on the reflectivity defined on it. From now on, we will refer to u^0 as the "preprocessed" signal (or data) and to G as the "reflectivity function". $\mathcal{E}\left(u(\mathcal{S}, G), u^0\right)$ is the error function (or misfit) between $u(\mathcal{S}, G)$ and u^0, i.e. the distance in the data space, which we will later cast in least squared form, while $(\mathcal{S}, G)$ corresponds to a point in the the parameter space (i.e. the space of all possible scene geometry and reflectivity combinations). The $R_\mathcal{S}$, R_G are regularisers to enforce smoothness on the shape and reflectivity function while α_1 and α_2 are weighting constants.

To build a successful inversion we must define a proper energy functional as smooth and convex as possible. Following Oliver (1989), there is direct connection between the time signature from a point scatterer and its location in space. Besides terms affecting amplitude, the echo of a LFM chirp produced by a single point scatterer (figure 1a), after conversion to baseband and pulse compression (figure 1b), corresponds to

$$\hat{\phi}\left(t', \tau_d\right) = sinc\left[\beta T\left(t' - \tau_d\right)\right] \exp\left(-i\omega_c \tau_d\right) \, , \tag{3}$$

where t' is time, τ_d is the round-trip delay-time, ω_c is the carrier frequency, and β is the chirp rate. τ_d may be related to the distance $r = \|\mathbf{x} - \mathbf{x}_a\|$ between the locations of the point scatterer $\mathbf{x}$ and the antenna by $\tau_d = 2r/C$ (with C denoting the speed of light). This allows us to switch between time and range. In the following, we will often use range to label the figures' horizontal axis, as its interpretation is more intuitive with respect delay time. We can expect the echo from the entire object to be well modelled as a superposition of terms like (3). When we introduced the cycle skip phenomenon, we highlighted that a least squared minimisation built on differences between oscillating functions leads to an energy possessing numerous local minima, and that this problem worsens as the frequency increases. Therefore, we can easily anticipate that the corresponding energy functional would present an intractable number of local minima if raw data were considered as they are. Intuitively, to be in the basin of attraction of the global minimum would require providing an initial shape within a few wavelengths (λ) of distance from the true model. In other words, we would

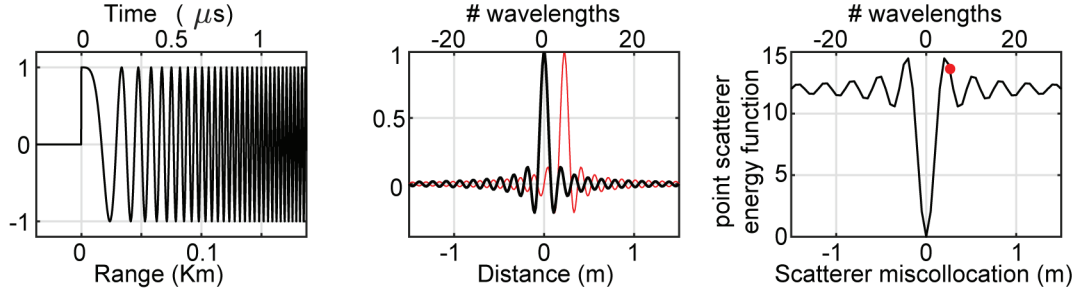*Radar-Based Reconstruction Using Variational Methods*

8

Figure 1. (a) Example of Linear Frequency Modulated signal in the C band (LFM up-chirp). Frequency increases from $f_{min} = 4\,GHz$ to $f_{max} = 6\,GHz$ (wavelength $\lambda \in [5, 7.5]\,cm$), over a $50\mu s$ active time (first $1.5\,\mu s$ are shown). (b) Signature of a point scatterer. The result after pulse-compression on the LFM signal shown in (a), corresponding to equation (3) computed at $\tau_d = 0$, is shown in black. The same pulse, delayed by 4.5 periods ($\tau_d = 4.5/f_{min}$), i.e. about $22.5\,cm$ apart, is shown in red. (c) Example of energy function (equation 1) for the simple case of a lone point scatterer scene, as a function of the distance between the true location of the scatterer and the initial input provided to a hypothetical inversion. The red dot shows the energy location corresponding to signals in figure (b), where $\mathbf{u}$ and $\mathbf{u}_0$ are associated to the red and black line, respectively. Despite the small delay, configuration in (b) is already in the basin of attraction of a local minimum. Notably, energy is dramatically non-convex and the multiple narrow local minima are the practical manifestation of cycle skipping at such high frequencies. Under these conditions, inversion would remain trapped around the initial model and fail.

already know the shape. For example, let's consider a scene consisting of just one point scatterer probed using the C-band LFM chirp of figure 1 (frequency band 4-6 GHz and pulse duration 50 μs). The antenna is considered to be at a distance of 20 Km. Figure 1c shows the energy functional (equation 1), as a function of the distance of a hypothetical initial guess from the true location. Notably, not only does the function present numerous close local minima, but it is also not convex. In this simple example, the inversion would lead to the correct solution only if the initial model (i.e. the scatterer location) was chosen within four wavelengths (ca. 20 cm) from the true position. The red dot highlights the energy value computed using the black and red pulses of figure 1b as true and simulated signals, respectively. The initial guess is only 22.5 cm (4.5λ) from the true location, yet the inversion is already destined to an unwanted local minimum. Even worse, since minima are narrow and tightly packed, an inversion would barely move from the provided initial guess.

A consideration to make is that historically, radar imaging focused on achieving the maximum pixel-wise resolution, for which the coherent sum of signals like equation (3) is a fundamental element. The price is that at a very small scale, the constructive/destructive interaction of point spread functions from different point scatterers is responsible for the speckle formation. In contrast, such a level of resolution is not actually necessary for shape reconstruction. In fact, amending for the presence of speckle is the main reason why the Shape from Shadows approach (Thomas et al. 1989)

Radar-Based Reconstruction Using Variational Methods 9

requires strong regularisation, eventually resulting in lower resolution. Following this consideration, note that if we consider the squared form of equation (3) the term oscillating with ω_c cancels and we are left with

$$\mathcal{P}(t' - \tau_d) = \hat{\phi}\,\hat{\phi}^* = sinc^2\left[\beta T(t' - \tau_d)\right] . \tag{4}$$

Nevertheless, equation (4) still retains an oscillating behaviour that must be properly addressed. When the echo from the entire surface is considered, we can lessen the oscillations introduced by terms such as (4) by smoothing the signals with a moving averaging window. Therefore the back-scattered, pulse compressed echoes $\phi_a(\tau)$ recorded on the interval $[t_{min}, t_{max}]$ by antenna a will be preprocessed according to

$$u_a^0(t) = \frac{1}{\Delta T}\int_{t-\Delta T/2}^{t+\Delta T/2} \phi_a(t')\,\phi_a^*(t')\,w(t')dt' , \tag{5}$$

while the response of our model (i.e. the forward model) can be computed according to

$$u_a(t) = \frac{1}{\Delta T}\int_{t-\Delta T/2}^{t+\Delta T/2}\left[\int_\mathcal{S}\mathcal{V}\frac{G\mathcal{R}w(t - \tau_d(r))}{r^4}\,\mathcal{P}(t' - \tau_d)d\mathcal{S}\right]dt' , \tag{6}$$

where ΔT is the window's width, $\mathcal{V}$ is a binary visibility indicator function along the surface, $\mathcal{R}$ is a radiative function which accounts for how the energy is absorbed/irradiated by the surface and w is a temporal averaging window.

Since the evolution of a general three-dimensional surface is particularly involved (the subject of a future paper in which Level Set Methods will be exploited for more general surface modelling flexibility), for the purposes of the present investigation we consider a simplified approach in which the surface is modelled as the graph of a function $z(x, y)$, i.e. $\mathcal{S}(x, y) = (x, y, z(x, y))$, representing heights over a fixed 2D spatial domain $\Omega \subset \Re^2$. In turn this allows us to similarly parameterise the various functions defined on the surface $\mathcal{S}$ as follows:

$$
\begin{aligned}
z &: \Omega \to \mathbb{R} &&= z(x, y) , \\
\mathcal{S} &: \Omega \to \mathbb{R}^3 &&= \mathcal{S}(x, y) = (x, y, z(x, y)) \\
\mathbf{N} &: \Omega \to \mathbb{R}^3 &&= N(x, y) = \left(\frac{\partial z}{\partial x}, \frac{\partial z}{\partial y}, 1\right) \Big/ \left\|\left(\frac{\partial z}{\partial x}, \frac{\partial z}{\partial y}, 1\right)\right\| , \\
r &: \Omega \to \mathbb{R} &&= r(x, y) = \sqrt{(x - x_a)^2 + (y - y_a)^2 + (z(x, y) - z_a)^2} , \\
G &: \Omega \to \mathbb{R} &&= G(x, y) , \\
\mathcal{R} &: \Omega \to \mathbb{R} &&= \mathcal{R}(x, y) \quad \dots \quad \text{may depend on both } \mathcal{S}(x, y) \text{ and } \mathbf{N}(x, y) , \\
\tau_d &: \Omega \to \mathbb{R} &&= \tau_d(x, y) = \frac{2\,r(x, y)}{C} ,
\end{aligned}
\tag{7}
$$

where $\mathbf{N}$ is the unit outward normal, and the integral of any generic function f on the evolving domain $\mathcal{S}$ (or on a portion of the same), can be rewritten as:

$$\int_\mathcal{S} f\, d\mathcal{S} = \int_\Omega f\, \|J\|\, d\mathbf{x} , \tag{8}$$

Radar-Based Reconstruction Using Variational Methods 10

where $\|J\| = \sqrt{1 + (\partial z/\partial x)^2 + (\partial z/\partial y)^2}$ is the Jacobian of the change from the surface area $d\mathcal{S}$ to the 2D spatial measure $d\mathbf{x}$. Finally, we are ready to introduce the explicit form of our energy functional as:

$$E = \sum_a^A \left\| u_a - u_a^0 \right\|^2 + \frac{\alpha_1}{2} \int_{\mathcal{S}} \|\nabla z\|^2 \, d\mathcal{S} + \frac{\alpha_2}{2} \int_{\mathcal{S}} \|\nabla G\|^2 \, d\mathcal{S}, \qquad (9)$$

where the functional norm $\|\cdot\|$ is built from its related inner product $<\cdot, \cdot>$ as follows

$$\langle f_1, f_2 \rangle = \int_{t_{min}}^{t_{max}} f_1(t) f_2^*(t) dt, \qquad \|f\|^2 = \int_{t_{min}}^{t_{max}} f(t) f^*(t) dt. \qquad (10)$$

Equations (5)-(10) define our inversion framework. It is particularly worth noting that in this form, the shape reconstruction problem is formulated in terms of signal amplitudes, while the "phase curtain" (Barnes 2015), classically leveraged by SAR imaging is actually not used. While this aspect may seem strange to a SAR expert, we must emphasise that by posing the problem in the inversion framework and providing an initial explicit shape to be optimised, we leverage information that is not available in traditional approaches. On the one hand, dropping the coherent summation forces us to perform the reconstruction to a lower resolution with compared to traditional SAR. On the other hand, we gain the capability of using sparse antennas and avoid limitations at very high frequencies.

In equation 6, the integral over a time window centred at t, translates to a sample of the simulated preprocessed signal. Geometrically, such a time window identifies two spherical shells of radius $\frac{C}{2}(t - \Delta T/2)$ and $\frac{C}{2}(t + \Delta/2)$, and the echo from the portion of surface included within these shells provides the most significant contribution to the simulated sample. Nevertheless, the support of $\mathcal{P}$ is in general wider than any practical choice of averaging window and the tails of this function, leaking outside the present window span, are captured within neighbouring time windows and in turn, contribute to neighbouring samples of the preprocessed signal. Conversely, part of the energy from neighbouring windows may leak into the present one. Recalling that we assumed the surface to be a continuous distribution of point scatterers, and recalling that the main lobe of the *sinc* function (equation 3) associated to each scatterer approximately spans half a wave length around its location, if the width of the averaging window is chosen large enough, the $sinc^2$ term (i.e. $\mathcal{P}$) may be substituted with the Dirac delta function and speckle does not need to be modelled.

Considering a realistic scene, this simplification implies that for a given finite portion of surface included in the above mentioned shells the cumulative effect of the $sinc^2$ tails leaking outside of the surface's borders (in terms of delay-time or range), should be negligible. Figure 2 summarises the result of a set of experiments performed to prove that this simplification is indeed acceptable. We considered a squared patch of $1 \, m^2$ containing a sufficiently high number of randomly placed point scatterers (10^4 in the shown example), so to simulate a dense, yet realistic, distribution. Antenna is assumed $20 \, Km$ far from the patch centre. Figure 2a shows an example from the 10^4 configurations generated by randomly placing 10^4 point scatterers. Subsequently, we
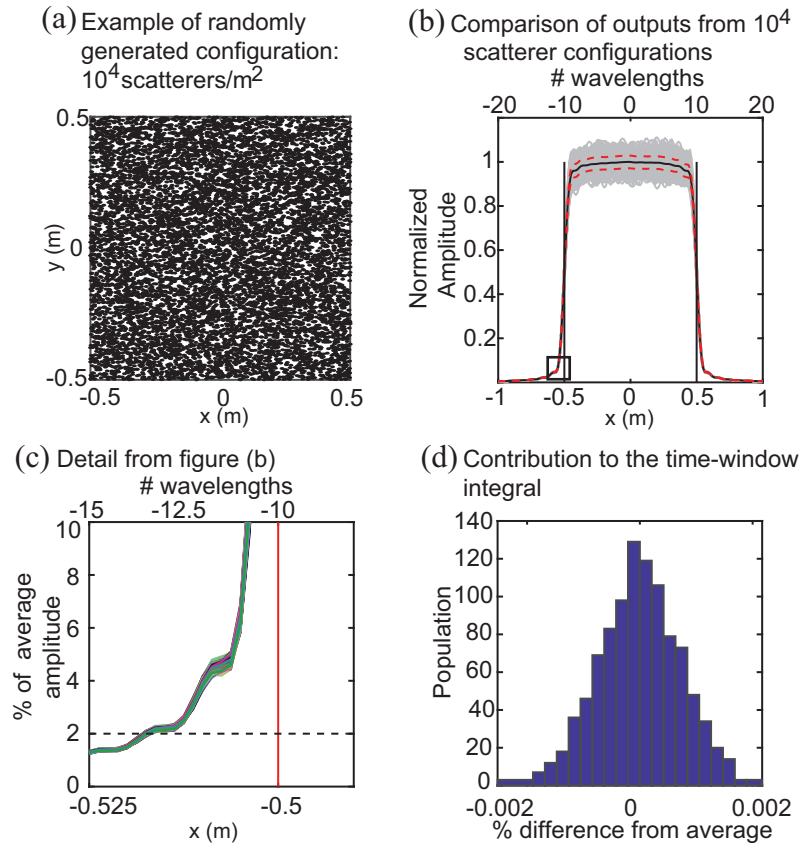
Figure 2. Experiment confirming that the term $\mathcal{P}$ in equation (6) can be substituted with a Dirac delta. a) Example of 10^4 randomly generated scatterers. b) Comparison of functions $\phi\phi^*$ (i.e. the quantity being integrated in equation 5) computed from individual signals ϕ backscattered by the 10^4 scatterer configurations like the one shown in (a), which highlights the change of regime at the distribution boundary. In all figures within this group delay times were converted to range as well as multiples of the wave length. Radar parameters are the same as figure 1. The solid black line and the dashed red lines represent average and standard deviation, respectively. c) Detail of figure (b). Showing that beyond the patch boundary tails of the signal fall under 2% of the maximum amplitude within 2-3λ distance (few cm) and therefore are of negligible concern to our approach. d) Integral values of signals. Histogram shows the distribution of values around the average. Discrepancy is lower than 0.003%, demonstrating that the time-windowing strategy is robust to short-scale features (speckle).

computed the echo ϕ from all the different patches as a superposition of terms like equation (3), (same simulation parameters as in figure 1). Figure 2b shows (in grey and normalised) the function $\phi\phi^*$ computed for all the 10^4 scatterer configurations (i.e. the quantity being integrated in equation 5). The mean and the standard deviation are drawn in black and red, respectively. Ranges corresponding to the patch edges are highlighted and the average amplitude within this interval (A_0) is used as normalisation constant. Notably, even though these functions are quite chaotic at the small scale, two different regimes can clearly be observed. In particular, the amplitude suddenly drops

Radar-Based Reconstruction Using Variational Methods   12

at the patch's edge. Figure 2c shows a magnification of the small squared portion at the bottom left of figure 2b and shows that after just one wavelength (c.a. 5 *cm*) the amplitude is reduced to 5% of A_0, confirming that $sinc^2$ tails are indeed negligible and the use of the Dirac delta in place of $\mathcal{P}$ is justified. Additionally, these functions show almost identical integral values (computed according to equation 5), with difference smaller than 0.003% (figure 2d), confirming that the small-scale details of the scatterers distribution has negligible effect on the preprocessed signals. It is worth mentioning that in order to approximate a continuous distribution we repeated this experiment with increasingly larger numbers of point scatterers: 10^4, 10^5, 10^6, and 10^7; obtaining consistent results.

Moving forward, equation (9) represents the most general form of this optimisation problem, where both z and G are evolved from an initial guess. Nevertheless, as we will show later, given a reference shape the optimal G can actually be directly estimated. Therefore, in the following we will drop the optimisation of G and the corresponding regularising term.

Implementation of such an inversion approach requires to perform several design choices: 1) since the scene is a graph of a function, we must adopt a suitable boundary condition at the surface edges. 2) decide which kind of averaging window is acceptable and 3) establish the correct radiative model. In the following we will discuss these aspects. Finally, due to the difficulty of obtaining a real-world dataset suitable for such a unconventional radar data inversion, we illustrate the capabilities of our approach through numerical simulations.

2.1. PDE-based variational approach

To obtain the evolution in the form of a continuous gradient descent PDE, we consider the unknown function z to lie along a continuously deforming family of functions $z(x, y, \tau)$ where the additional variable τ parameterises the family. As such, the energy functional evaluated along this evolving family of functions now becomes a simple scalar function of τ, whose derivative may be expressed in the following integral form (following the same mathematical development taken, for example, in Kichenassamy et al. 1995, Yezzi et al. 1997),

$$\frac{\partial E}{\partial \tau} = \int_\Omega \underbrace{(\cdots)}_{\nabla_z E} \frac{\partial z}{\partial \tau} \, d\mathbf{x} \,, \tag{11}$$

where all partial derivatives with respect to τ inside the integral are isolated via combinations of the chain rule and integration by parts into the single term $\frac{\partial z}{\partial \tau}$ shown above. The remainder of the integrand, which we denote by $\nabla_z E$ represents the functional derivative of E (which, when set to zero, yields the classical Euler-Lagrange equation from the Calculus of Variations) also known as the first variation. It can be interpreted as an infinite dimensional gradient of E over the space of all possible functions z (not to be confused with the two-dimensional spatial gradient of the function

Radar-Based Reconstruction Using Variational Methods   13

z itself) with respect to the standard functional L^2 inner product and/or norm. As such, we need to develop and manipulate

$$\frac{\partial E}{\partial \tau} = \sum_{a=1}^{A} \int_{t_{min}}^{t_{max}} \left(u_a(t) - u_a^0(t) \right) \frac{\partial u_a(t)}{\partial \tau} \, dt + \frac{\alpha_1}{2} \frac{\partial}{\partial \tau} \int_{\mathcal{S}} \|\nabla z\|^2 \, d\mathcal{S}. \tag{12}$$

For simplicity, let's first consider the derivative $\partial u_a(t)/\partial \tau$. Let's define $\mathcal{Q} \doteq \{\mathbf{x} \,|\, (C/2)\,(t - \Delta T/2) \leq r \leq (C/2)\,(t + \Delta T/2)\}$, the portion of $3D$ space corresponding to delay times $\tau_d \in [t - \Delta T/2, t + \Delta T/2]$. It can be demonstrated that, using a delta function in place of $\mathcal{P}$, for a specific instant t, integral (6) can be rewritten as the integral on the portion of surface $\mathcal{S} \cap \mathcal{Q}$.

$$u_a(r) = \frac{1}{\Delta T} \int_{\mathcal{S} \cap \mathcal{Q}} \mathcal{V} \frac{Gw\mathcal{R}}{r^4} \, \|J\| \, dx \, dy, \tag{13}$$

Considering dependencies in equations (7), we obtain:

$$\begin{aligned}
\frac{\partial u_a(r)}{\partial \tau} = \frac{1}{\Delta T} \Bigg[& \int_{\mathcal{S} \cap \mathcal{Q}} -4\mathcal{V} \frac{Gw}{r^5} \mathcal{R} \, \|J\| \, \frac{\partial r}{\partial z} \frac{\partial z}{\partial \tau} \, dx \, dy \\
& + \int_{\mathcal{S} \cap \mathcal{Q}} \mathcal{V} \frac{Gw}{r^4} \left(\frac{\mathcal{R}}{\|J\|} \frac{\partial z}{\partial x} + \frac{\partial \mathcal{R}}{\partial z_x} \|J\| \right) \frac{\partial^2 z}{\partial x \partial \tau} \, dx \, dy \\
& + \int_{\mathcal{S} \cap \mathcal{Q}} \mathcal{V} \frac{Gw}{r^4} \left(\frac{\mathcal{R}}{\|J\|} \frac{\partial z}{\partial y} + \frac{\partial \mathcal{R}}{\partial z_y} \|J\| \right) \frac{\partial^2 z}{\partial y \partial \tau} \, dx \, dy \\
& + \int_{\mathcal{S} \cap \mathcal{Q}} \mathcal{V} \frac{Gw}{r^4} \frac{\partial \mathcal{R}}{\partial z} \|J\| \frac{\partial z}{\partial \tau} dx \, dy + \int_{\mathcal{S} \cap \mathcal{Q}} \mathcal{V} \frac{G}{r^4} \frac{\partial w}{\partial r} \mathcal{R} \, \|J\| \, \frac{\partial r}{\partial z} \frac{\partial z}{\partial \tau} \, dx \, dy \Bigg],
\end{aligned} \tag{14}$$

where for sake of simplicity we used $z_x = \partial z / \partial x$, and $z_y = \partial z / \partial y$. Swapping the order of derivatives in $\partial^2 z / \partial x \partial \tau$ and $\partial^2 z / \partial y \partial \tau$, integrating by parts the second and third line of (14), then collecting all the terms in one integral, we obtain a very interesting result:

$$\begin{aligned}
\frac{\partial u_a(r)}{\partial \tau} = \frac{1}{\Delta T} \int_{\mathcal{S} \cap \mathcal{Q}} \mathcal{V} \Bigg\{ & \frac{Gw}{r^4} \frac{\partial \mathcal{R}}{\partial z} \|J\| + \frac{G}{r^4} \frac{\partial w}{\partial r} \mathcal{R} \|J\| \frac{\partial r}{\partial z} - \frac{4Gw}{r^5} \mathcal{R} \|J\| \frac{\partial r}{\partial z} \\
& - \frac{d}{dx} \left[\frac{Gw}{r^4} \left(\mathcal{R} \frac{\partial \|J\|}{\partial z_x} + \frac{\partial \mathcal{R}}{\partial z_x} \|J\| \right) \right] - \frac{d}{dy} \left[\frac{Gw}{r^4} \left(\mathcal{R} \frac{\partial \|J\|}{\partial z_y} + \frac{\partial \mathcal{R}}{\partial z_y} \|J\| \right) \right] \Bigg\} \frac{\partial z}{\partial \tau} \, dx \, dy \\
& + \left[\frac{Gw}{r^4} \mathcal{V} \left(\mathcal{R} \frac{\partial \|J\|}{\partial z_x} + \frac{\partial \mathcal{R}}{\partial z_x} \|J\| \right) \frac{\partial z}{\partial \tau} \right]_{x_{min}}^{x_{max}} + \left[\frac{Gw}{r^4} \mathcal{V} \left(\mathcal{R} \frac{\partial \|J\|}{\partial z_y} + \frac{\partial \mathcal{R}}{\partial z_y} \|J\| \right) \frac{\partial z}{\partial \tau} \right]_{y_{min}}^{y_{max}},
\end{aligned} \tag{15}$$

Third line in equation (15) is a complicated boundary term which should either vanish or be carefully handled. Actually, a straightforward solution is to select a time windowing function w that vanishes at the extrema of its interval of definition. Consequently, from now on, we use a triangular windowing function. Inserting (15) in equation (12), we

Radar-Based Reconstruction Using Variational Methods 14

obtain

$$
\frac{\partial E}{\partial \tau} = \frac{1}{\Delta T} \sum_{a=1}^{A} \int_{t_{min}}^{t_{max}} \left(u_a(t) - u_a^0(t) \right) *
$$

$$
\int_{\mathcal{S}} \chi_{\mathcal{Q}} \mathcal{V} \left\{ \frac{Gw}{r^4} \frac{\partial \mathcal{R}}{\partial z} \| J \| + \frac{G}{r^4} \frac{\partial w}{\partial r} \mathcal{R} \| J \| \frac{\partial r}{\partial z} - \frac{4Gw}{r^5} \mathcal{R} \| J \| \frac{\partial r}{\partial z} \right.
$$

$$
- \frac{d}{dx} \left[\frac{Gw}{r^4} \left(\mathcal{R} \frac{\partial \| J \|}{\partial z_x} + \frac{\partial \mathcal{R}}{\partial z_x} \| J \| \right) \right]
$$

$$
\left. - \frac{d}{dy} \left[\frac{Gw}{r^4} \left(\mathcal{R} \frac{\partial \| J \|}{\partial z_y} + \frac{\partial \mathcal{R}}{\partial z_y} \| J \| \right) \right] \right\} \frac{\partial z}{\partial \tau} \, dx \, dy \, dt
$$

$$
- \alpha_1 \int_{\mathcal{S}} \triangle z \, \frac{\partial z}{\partial \tau} \, d\mathcal{S}, \tag{16}
$$

where we used the indicator function

$$
\chi_{\mathcal{Q}}(\mathbf{x}) \doteq \begin{cases} 1 & \text{if } \mathbf{x} \in \mathcal{Q}, \\ 0 & \text{otherwise}, \end{cases} \tag{17}
$$

to rewrite the integral on $\mathcal{S} \cap \mathcal{Q}$ as an integral over the whole surface $\mathcal{S}$. We can recognise that if we now swap the space and time integrals, equation (16) has the form (11), with

$$
\nabla_z E = \frac{1}{\Delta T} \sum_{a=1}^{A} \int_{t_{min}}^{t_{max}} \left(u_a(t) - u_a^0(t) \right) *
$$

$$
\chi_{\mathcal{Q}} \mathcal{V} \left\{ \frac{Gw}{r^4} \frac{\partial \mathcal{R}}{\partial z} \| J \| + \frac{G}{r^4} \frac{\partial w}{\partial r} \mathcal{R} \| J \| \frac{\partial r}{\partial z} - \frac{4Gw}{r^5} \mathcal{R} \| J \| \frac{\partial r}{\partial z} \right.
$$

$$
\left. - \frac{d}{dx} \left[\frac{Gw}{r^4} \left(\mathcal{R} \frac{\partial \| J \|}{\partial z_x} + \frac{\partial \mathcal{R}}{\partial z_x} \| J \| \right) \right] - \frac{d}{dy} \left[\frac{Gw}{r^4} \left(\mathcal{R} \frac{\partial \| J \|}{\partial z_y} + \frac{\partial \mathcal{R}}{\partial z_y} \| J \| \right) \right] \right\} dt \bigg|_{\mathbf{x}}
$$

$$
- \alpha_1 \triangle z, \tag{18}
$$

Equation (18) is the general form of the gradient, valid continuously at each point on the surface, which we use to obtain the following continuous gradient descent PDE

$$
\frac{\partial z}{\partial \tau} = -\nabla_z E. \tag{19}
$$

Finally, this PDE may be discretised in the variable τ to obtain the desired shape update steps:

$$
z^{\tau+1} = z^{\tau} - \alpha \nabla_z E, \tag{20}
$$

$$
z^{\tau+1} = z^{\tau} - \alpha \left[(1 - \alpha_{acc}) \nabla_z E + \alpha_{acc} \nabla_z E^{\tau-1} \right], \tag{21}
$$

depending if the regular (20) or the accelerated gradient descent (21) is used. Constant α in equations (20) and (21) being the step of the gradient descent, and α_{acc} the amount of acceleration. It is worth of note that, the use of the accelerated gradient descent reduced the computational times of about 90%, so that in practice, throughout this paper we used only the accelerated descent.
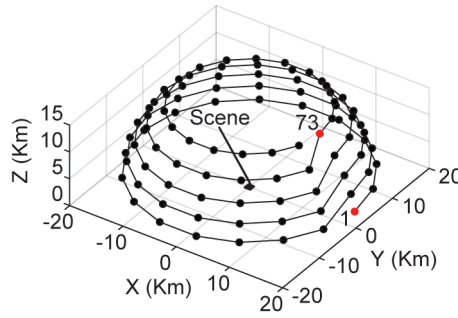
Radar-Based Reconstruction Using Variational Methods 15

Figure 3. Reference geometry for experiment 1 and 2. Dots represent 90 antenna distributed on a semi-spherical surface with 20 Km radius (18 equispaced locations on 5 height levels). At each location a radar signal is emitted, and the corresponding echo from the scene, centred on the axes origin, is recorded.

3. Results

In the following, we consider three different test inversions. In examples 1 and 2, we consider a set of 90 antenna locations distributed at 5 height levels on a spherical surface with radius 20 Km (Figure 3). The scene is a 1 Km by 1 Km hill possessing a Gaussian profile and 100 meters high at its centre. The probing signal is assumed to be a LFM chirp, frequency band 4-6 GHz and 5 μs pulse duration.

In example 1, figures 4 and 5, the radiative function assumed on the surface is the exploding reflector $\mathcal{R} = 1$ and G is known. Rather, example 2, figures 6-8, features the Lambertian radiative function $\mathcal{R} = (\mathbf{e}_r \cdot \mathbf{N})^2$, with $\mathbf{e}_r = \mathbf{r}/\|\mathbf{r}\|$. As such both the incident and the re-irradiated signals have an amplitude proportional to the cosine between the ray from the antenna to the surface and the normal vector to the surface. Finally, example 3 (figures 9-13) leverage $\mathcal{R} = (\mathbf{e}_r \cdot \mathbf{N})$. In addition, in this last experiment the effect of noise contaminating the data is considered. The practical implementation requires to substitute the various radiative assumptions $\mathcal{R}$ into (18) and explicitly compute the corresponding final forms. Explicit derivations of $\nabla_z E$ according to different radiative assumptions is somewhat lengthy but conceptually simple. As such, we summarise the final formulas in Appendix A. Further, for computational purposes, we need now to discretise equation (18). To do so, the surface is densely sampled over a regular grid, in such a way that we can assume each surface sample to be well approximated by a scatterer of area dA. Therefore, the first advantage of using the PDE approach is that, by considering the surface as a dense collection of discrete scatterers of very small area (compared to the size of the averaging triangular window), we avoid the numerical issue of quadrature integration along individual finite elements. Returning to the examples, figure 4 shows few snapshots of the obtained surface evolution. As it can be observed, results are extremely good. In fact, the error in evaluating z is lower than 2%. Further, the only intervention we performed was lowering the weight for the regulariser α_1, once. The values of the parameters used for the minimisation in this and following examples are summarised in table 1. Figure 5a

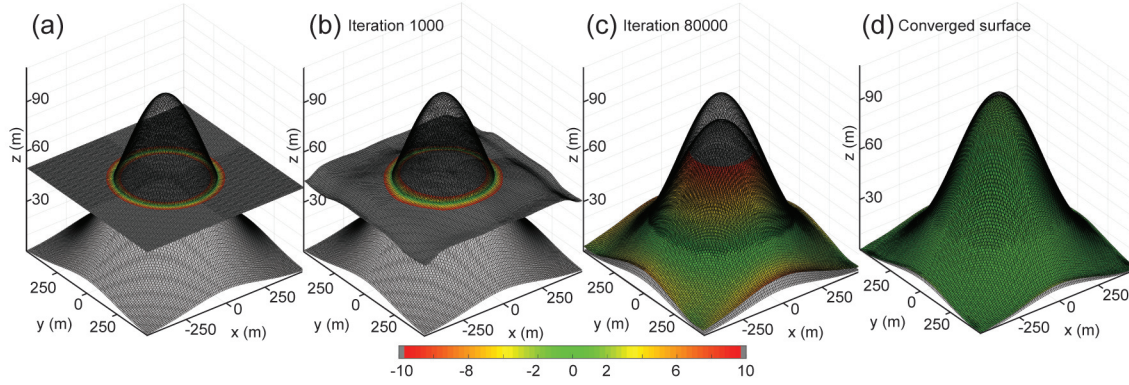*Radar-Based Reconstruction Using Variational Methods*   16

Figure 4. Result in the space of models. True and evolving surfaces are shown as frame and coloured, respectively. Reflectivity is constant ($g = 0.71$) and known a-priori. Colours indicate the distance (in m) from the true shape.
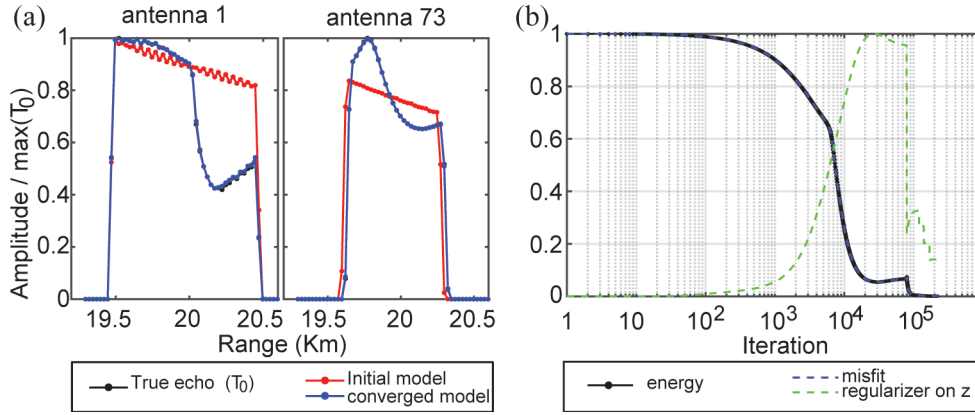

Figure 5. a) Result in the space of data concerning selected antennas in figure 3). b) Minimization of the energy functional.

Table 1. Summary of the parameters values used in the provided examples and their changes with iterations.

	iteration	α	α_1	α_{acc}
Example 1	1	1×10^{23}	0.1	0.9
	8×10^4	1×10^{23}	0.0125	
Example 2	all	1×10^{22}	0.1	0.9
Example 3	all	100	1×10^{-5}	0.9

shows the averaged, normalised windowed echoes at antenna locations 1 and 73. We selected these two specific locations because they represent the extreme cases in terms of elevation, while other location on the same levels are almost cylindrically symmetric. Finally, figure 5b shows the corresponding energy minimisation. In example 2, (figure 6) shape reconstruction is performed based on a Lambertian radiative assumption and an unknown, potentially variable across the surface, reflectivity. As previously mentioned, given a scene geometry it is simple to devise a strategy to estimate G. In
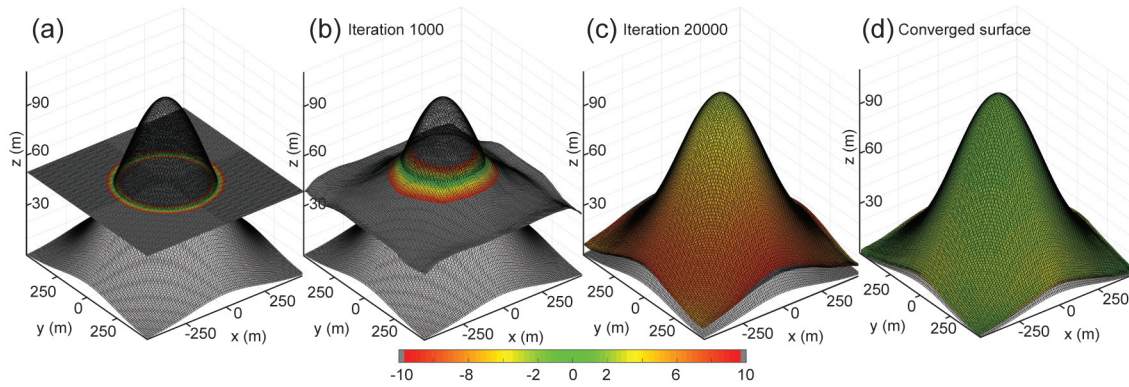
Figure 6. Result in the space of models. True and evolving surfaces are shown as frame and coloured, respectively. Colours indicate the distance (in m) from the true shape.
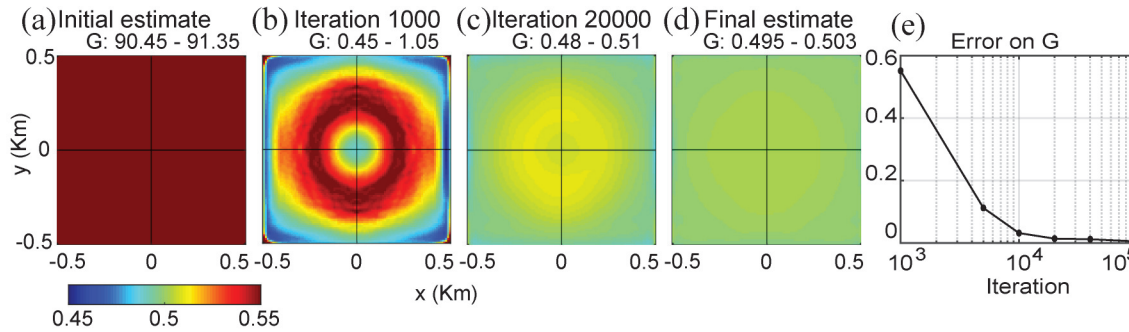

Figure 7. Result in the space of models. True reflectivity is constant ($G = gg^* = 0.5$), while the value across to the evolving surface is estimated using the algorithm in Appendix B.1. a) to d): Estimated G. e) Error with respect the true G.

this example we used an algorithm that considers G as piecewise constant (details in Appendix B.1). Figure 7a-d show the estimates of G across the surface corresponding to images 6a-d. Elevation z is reconstructed with an error lower than 3%. Further, the algorithm reproduced the true, constant $G = 0.5$ within 1% discrepancy. Figure 7e shows the maximum difference in terms of G between the true and the reconstructed model. Figures 8a shows the result in terms of data matching for the two selected antenna locations. Of course, such signals are different from the previous example, as they are based on a different radiative model. The Lambertian introduces a stronger constraint on the shape than the exploding reflector model. As such it is of no surprise that the energy minimisation (figure 8b) looks smoother. Indeed, no intervention was required to achieve the latter result. The slightly lower performance in retrieving z is motivated by the fact that a piecewise reflectivity violates the requirement of a smooth G and introduces, to some degree, instability of the gradient descent flow. In this particular example however, such instability was compensated by the good illumination provided by the high number of antenna locations. In our last experiment, inspired to a hypothetical acquisition performed by a unmanned aerial vehicle (e.g. a remotely
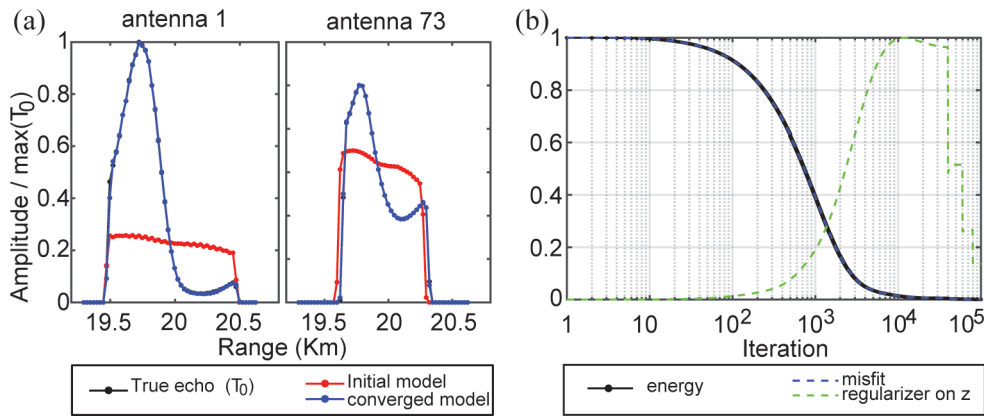
Radar-Based Reconstruction Using Variational Methods   18

Figure 8. a) Result in the space of data concerning selected antennas in figure 3). b) Minimisation of the energy functional.
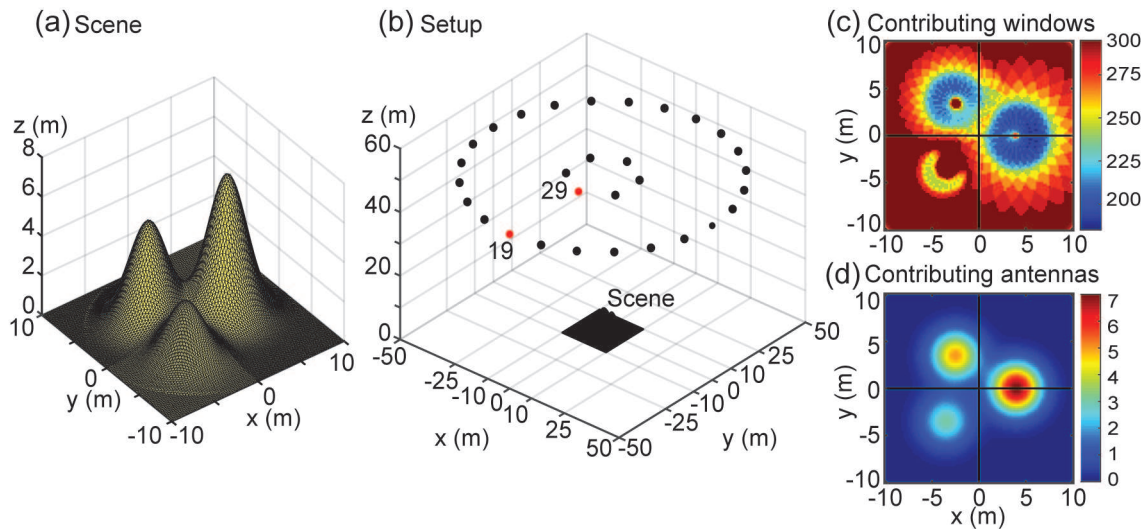

Figure 9. Experiment 4. a) True scene. b) Antenna locations. c) and d): number of time windows and antennas sensing different parts of the scene.

controlled quadcopter), hovering on the scene, we consider the geometry of figure 9a. The scene, in this case, is a small 10 m by 10 m patch, and features three spikes of variable heights (2, 5 and 7 meters), purposely designed to generate a challenging to reconstruct scenario and where the scene visibility is partially occluded to some antennas. The reflectivity of the true scene is constant ($G = 0.5$). Antenna locations are, on average 50 meters above the scene (figure 9b). Figures 9c and 9d show a top view of the surface, where the colour code represents the total number of time-windows and antennas sensing different portions of the surface. In other words, they represent the "sensitivity" of data to the scene geometry. In this case the radiative model is $\mathcal{R} = (\mathbf{e}_r \cdot \mathbf{N})$. Beside greatly simplifying the expression of the gradient flow, this model is in our perspective the most physically sound for the inversion of radar backscattered electric field. The interested reader may refer to Yildirim (2019) for rigorous proof. In

this inversion the reflectivity is unknown initially. We dynamically estimate the best value of a constant reflectivity while optimising the shape. This approach guarantees a sufficiently good estimation of the reflectivity while preserving the smooth reflectivity constrain. The analytical solution for the calculus of G is provided in equation (B.13). An additional motivation behind this assumption is that for full 3D active surfaces using level set methods applications (for which this study is preparatory), where changes of topology are naturally handled and the surface may split into different disjoint shapes, it is simple to manage scenes composed of multiple constant-reflectivity objects. These aspects however represent future work and will not be discussed here. In contrast with the previous examples, this experiment addresses the role of noise affecting the data and its impact on the shape reconstruction. It is worthy of note that since the noise is of a stochastic nature, we expect it will be greatly attenuated by the time averaging used in equation (5). To quantify this effect, we performed a small experiment. The surface in figure 9a. is defined on a 0.2 by 0.2 meter grid, while the width of the triangular time window used to compute (5) is 0.5 meters. As such, similar to the example in figure (2), we considered a random distribution of point scatterers with a density of 25×10^6 $points/m^2$ along a hypothetical surface patch of size 0.2×1.5 meters. We computed the echo generated by this distribution of scatterers (via superposition of terms as in equation 3), assuming the antenna to be located 50 meters away from its centre, in a direction aligned with the longitudinal axis of the patch. The LFM chirp emitted by the antenna is chosen with frequency band 4-6 GHz and pulse duration 0.1 μs. With this computed echo as a reference, we used randomly generated, zero-mean Gaussian noise to create 50000 instances of noisy data, each with signal to noise ratio (SNR) of about 20 dB. Such noise was designed to corrupt both amplitude and phase randomly. Figure 10a shows the ratio between the width of the triangular window and the grid spacing of the surface, as well as how the *sinc* (in black) and $sinc^2$ (in red) functions (equation 4), for one scatterer, fit within this range span. For each simulated noisy signal we computed the corresponding processed signal (5, the quantity we invert for) and the signal to noise ratios before and after processing. Figure 10b compares the distribution of these SNR. The vertical axis, denoted "probabilit" represents the height of the histogram bars divided by the total population (i.e. 50000). After processing, the initial SNR (20 dB) greatly improves. However, to further emphasize the robustness of our approach to noise, in this example we will assume that noise with 20 dB SNR has not been mitigated by the time windowing. Figure 11 shows the evolution flow starting from an initial parabolic shape. In this experiment we imposed Dirichlet (i.e. $z=0$) boundary conditions. The correct shape is recovered almost perfectly, except few sparse locations which present a maximum error of 2%. We easily discriminated the three spikes in the scene and despite the visibility occlusions, correctly reconstructed their different heights and curvy tips. Figure 12 shows the evolution of the estimated reflectivity of the scene. The first estimate, even if the starting shape was completely different, was only 4% off. Subsequently, it evolved concurrently with the shape and finally reached a value 0.3% off with respect to the true value. Finally, figures 13a
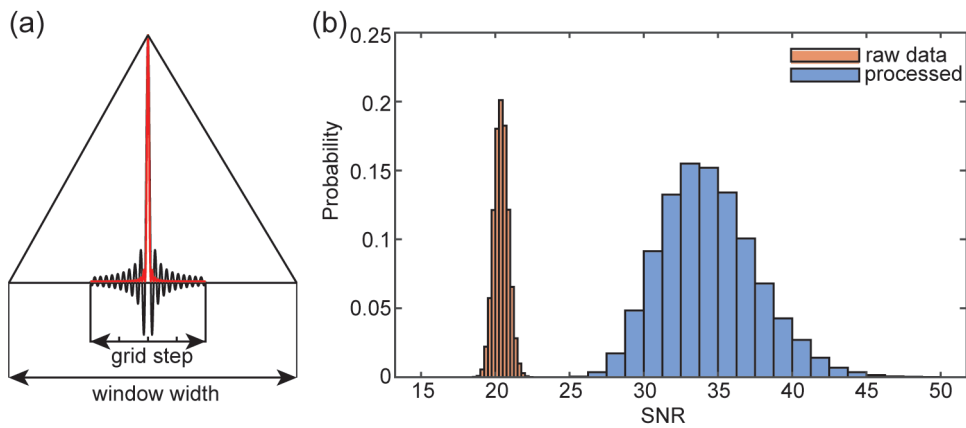
Radar-Based Reconstruction Using Variational Methods   20

Figure 10. Investigating the effect of noise under the modelling conditions of example 3 (figure 9). The echo from a portion of surface containing a random distribution of point scatterers is used to compute a reference echo, which in turn is used to generate 50000 instances of noisy data. Subsequently, the observable function (equation 5) and SNR before and after processing are computed. a) shows the ratio between the grid spacing of model 9a, width of the triangular window, and the $sinc$ (black) and $sinc^2$ (red) functions associated to one point scatterer (all expressed in terms of range). b) comparison of SNR before (raw data) and after processing showing how the noise is greatly attenuated.
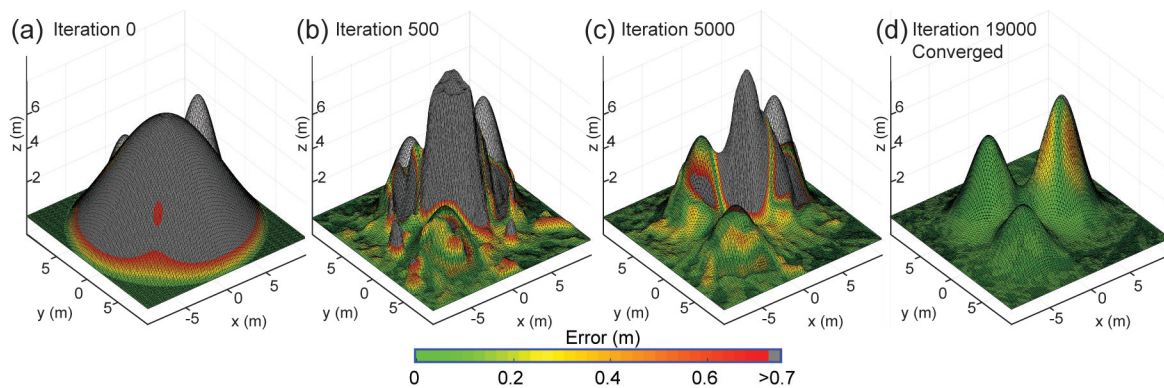

Figure 11. Result in the space of models. True and evolving surfaces are shown as frame and coloured, respectively. Colours indicate the distance (in m) from the true shape.
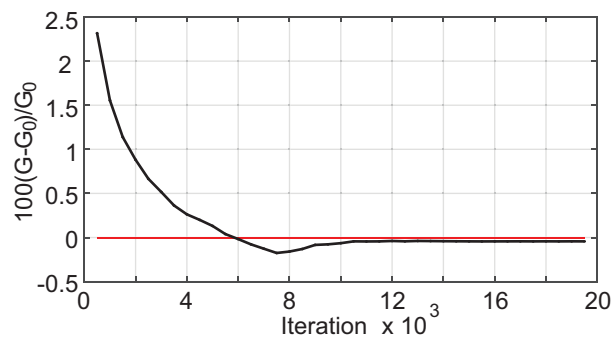

Figure 12. Result in the space of models. Percent difference between successive estimates of G using the analytical formula (B.13) and the true value $G_0 = 0.5$.
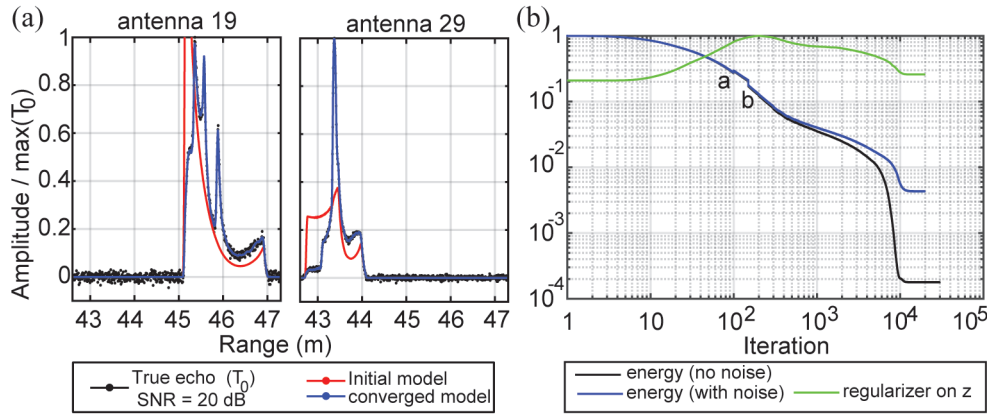
Figure 13. a) Result in the space of data concerning selected antennas in figure 9b. b) Minimisation of the energy functional.

shows the result, in the data domain. Despite the noise, we obtained an excellent fit. Energy, figure 13b, is nicely minimised without the need of any intervention on the inversion parameters. The high values of the regulariser in mid iterations (green dashed curve) show that the surface at intermediate iterations was highly irregular with complex visibility occlusions. Nevertheless, since totally occluded regions are still evolved by the regulariser, the inversion process is capable of recovering and if necessary, bring back to the correct visible location, those portions of the surface that could not evolve any more and would otherwise generate false positives. Small discontinuities in the energy, as highlighted by the a and b labels in figure 13b plot are due to adjustments in the estimated reflectivity. The effect of noise on the energy minimisation can be observed in figure 13b by comparing the energy minimisation associated with noisy data (blue line) to the noise free minimisation (black line). To highlight this difference, in this plot we used a logaritmic vertical scale, while difference in the reconstructed shape were almost undetectable.

4. Discussion

In section 3 we showed how to perform shape reconstruction by inverting time-domain radar echoes acquired at sparse locations. We achieved this by formulating the problem within a similar variational framework used for multiview stereo reconstruction, well established in computer vision to tackle shape inversion from image data acquired by sparse cameras. To do so, we built a least squared optimisation in which the mismatch is computed with respect an observable quantity (equation 5) derived from radar data. Since radar signals are oscillatory in nature, two key aspects of this equation are that it considers the power of the signal and it leverages a time averaging window. These two features together help suppress most of the oscillating terms, leading to a sufficiently well behaved energy. The advantage of the variational formalism is that the energy gradient is computed analytically, keeping the representation of the surface continuous, with

Radar-Based Reconstruction Using Variational Methods   22

discretisation introduced only at the very last stage for the sake of practical computation.

It is worth mentioning that in our earliest attempts to tackle this problem, we used a finite element approach in which the surface was discretised using triangular elements and each integration operation over it (e.g. equation 6) was performed numerically on each element. In addition we considered squared and Gaussian windows as time averaging strategy. Finally, reflectivity was known. This early approach was not successful when implemented using squared windows while it worked using Gaussian windows. Even when successful, the converged surface still presented errors in z up to 10%. In addition, to be practical the finite element approach required surface re-meshing and consequently, re-processing of raw data with different time window lengths. In other words, inversion required several manual interventions and involved parameter tuning. The PDE-based evolution provided striking improvement. Not only the necessity for remeshing was completely removed, but errors in z are lower than 3%, even when reflectivity is unknown. We also demonstrated that reflectivity can be estimated with errors lower than 0.5%. Notably, the result is achieved with little or no user intervention. In addition, the explicit presence of boundary terms in equation (15) highlighted by the variational analysis elegantly explains why the use of a square windows failed and why the result obtained with the Gaussian window, despite being reasonable, was only partially successful.

As highlighted in section (2) averaging the data with a moving time-window has several direct consequences. First, we do not exploit the phase curtain but we rather leverage the amplitude information, in terms of energy density located at specific ranges. We note, in some sense, that the information lost by disregarding the phase curtain is actually re-introduced in the inversion machinery by the fact that we are performing a local optimisation with respect to an explicitly modelled surface. In turn, this surface determines how the back reflected energy distributes over different ranges and it is then observed by the antennas, making the coherent summation unnecessary. Second, while the location of every portion of surface (and therefore the general shape), is mostly ruled by the presence of back-reflected energy at a specific delay time, the actual amount of such energy is ruled by the reflectivity and the radiative behaviour. In other words, we can still reconstruct the shape fairly well, even with a poor estimation of the reflectivity.

The price of using a sparse configuration of antennas (and abandoning phase summation) seems to be a loss of resolution, to some extent. However, such a loss is only an apparent issue. For example, Thomas et al. (1989) achieved topography reconstruction leveraging stereo reconstruction technique on SAR images using a "smoothness" regulariser to cope with speckle. They observed that strong regularisation was necessary for the reconstruction to succeed. In turn, the regularisation resulted in lower resolution. Their findings with stereo image reconstruction is by all means equivalent with what we observed dealing with independent echo signals and using an averaging window. The consideration to make is that to determine the shape of an object of interest, the high resolution provided by SAR images is actually unnecessary as objects are typically of a larger scale compared to images pixels.

In the present context, the resolution to which the scene geometry is reconstructed depends on the spacing of the computational grid and on the width and overlap (in terms of range) of the triangular windows used. Since we are dealing with a least-squared nonlinear optimisation, it is very difficult to quantify the resolution analytically. Nevertheless, if we consider a small patch of surface surrounding a point of the discretised surface $(x, y, z(x, y))$, the grid spacing should be chosen large enough to consider its collective contribution, as opposed to modelling all of the scatterers distributed on it. In figure (2) we demonstrated that the cumulative signal from an almost continuous distribution of scatterers on a patch is well behaved and the tails leaking outside the patch (in terms of range) are negligible after 2-3 wavelengths distance. In addition, considering a hypothetical point scatterer on this patch, the time window used to average the raw data should be chosen large enough to include the main lobe and few of the secondary lobes of the associated $sinc^2$ function (i.e. most of the energy re-irradiated by the scatterer). Ideally, this is achieved choosing a time-window as large as the grid spacing augmented by 4-6 wavelengths (to include oscillating tails). After these considerations, not accounting for squinted view angles from the antennas with respect to the orientation of the computational grid and disregarding the fact that each time window should cover a "sufficiently wide stripe of surface", it can be expected that achievable resolution may be as low as 10 wavelengths. Nevertheless, the loss in resolution introduced by the time averaging window can be partially recovered using partially overlapping windows. In fact, there is no limitation on the amount of such overlap. In example 3 for example, we considered a grid spacing and a window width equivalent to 4 and 20 wavelengths, respectively. Windows' overlap of 90% ensured that information within consecutive time-windows differed only by the contribution of a surface band 2 wavelengths wide (c.a. 10 cm). With the presence of a reference evolving surface our approach fully accounts for visibility, although we did not account for multiple scattering.

Within raw radar signals, the effect of multiple scattering is the presence of back scattered energy at later delay times. As far as the inversion approach is concerned, the use of several overlapping windows allows discriminating such energy from direct backscattering. Therefore, the only limitation in this sense, comes from the modelling routine underlying the inversion, which was not designed to account for this phenomenon. While the main motivation for this choice was to lower the computational cost, this choice was also motivated by the fact that smooth surfaces (such as those dealt here) are less prone to generate multiple reflections and when these occur, they are expected to be strongly attenuated. Summarising, accounting for multiple reflections would only require the use of a more involved forward model.

Finally, real world radar echoes contain usually some level of noise, which is typically a stochastic, zero mean phenomenon. Such noise affects the samples of the complex raw data, both in terms of amplitude and phase. Since traditional radar processing leverages phase summation, great effort is placed to achieve the best signal to noise ratio (SNR). In contrast, we leverage the backscattered energy density distribution as

Radar-Based Reconstruction Using Variational Methods 24

function of time/range. Noise may affect the amount of energy at a specific range but not its collocation in terms of range, which as we have shown rules our shape evolution. Additionally, we demonstrated that the noise in the raw data is strongly attenuated once the observables to be inverted are computed (equation 5). Given a fixed range, the surviving noise will manifest itself in a slight amplitude perturbation, and as explained before, in our approach this kind of perturbations don't impact the shape but rather affects the reflectivity. On the other hand, we have shown that we can estimate reflectivity on the fly and achieve the correct reconstruction even when such estimate is poor. Most importantly, we must emphasise that this inversion can tolerate uncertainties on reflectivity far greater than any noise related disturbance.

5. Conclusion

In this paper we tackled the problem of shape and reflectivity reconstruction from remotely sensed radar signals. In contrast with classic approaches, where the shape is retrieved using well established computer vision tools on images formed by traditional radar imaging, we formulated the problem as an iterative local inversion of the time-domain radar back-scattered signals. Key considerations concerning our approach and implementation aspects have been illustrated by means of three examples, with increasing complexity. Such implementation aspects include: 1) the strategy adopted in order to form a well-behaved energy functional from such high frequency signals in order to avoid the cycle-skipping phenomenon. We solved this difficulty by means of a moving averaging window, and we motivated why such windows must be of finite length and fade to zero at their end points. 2) we investigated three different radiative models of the surface, 3) we illustrated strategies to directly evaluate the reflectivity of the surface. 4) since for simplicity we limited our investigation to surfaces defined as a graph of a function, we used two different boundary conditions. 5) Finally, we discussed the mechanisms ruling the model evolution, the achievable resolution and robustness with respect to noise. The result of this investigation is therefore that in order to build a well behaved energy functional an averaging strategy of the raw signals should be adopted. This choice has several direct consequences. First, we do not exploit the phase curtain but we rather leverage the amplitude information, in terms of energy density located at specific ranges. We note, in some sense, that the information lost by disregarding the phase curtain is actually re-introduced in the inversion machinery by the fact that we are performing a local optimisation with respect to an explicitly modelled surface. In turn, this surface determines how the back reflected energy distributes over different ranges and how it is observed by different antennas, making the coherent summation unnecessary. As such, this can be considered a noncoherent approach.

This approach extends the useful processing range for data collected by sparse antennas and high frequencies. We showed that shape can be accurately reconstructed even with a poor estimation of the reflectivity and that reflectivity can be accurately evaluated knowing the shape. The problem is particularly simple if a constant reflectivity

Radar-Based Reconstruction Using Variational Methods   25

is assumed. Therefore, despite the restriction in this study to surfaces parametrized as a graph, we demonstrated that variational approaches leading to PDE driven shape evolution represent a natural and elegant framework to reconstruct scene geometry. Given these results, extending the present mathematical framework to more general 3D active surfaces and expressing the surface in more flexible implicit form using level set methods would be the most promising and natural next step to advance this variational framework. Level set methods will naturally handle changes of surface topology and will allow for the presence of different constant-reflectivity objects coexisting in the same scene even if their number is a-priori unknown. This will indeed be a key focus of our upcoming future work.

Acknowledgements

Appendix A. Explicit forms of the gradient flow

In section 2.1 we provided the most general form of $\partial u(r)/\partial \tau$ equation (15), and we introduced it into the energy derivative (12). Subsequently, we defined the indicator function χ (17) to swap the time and surface integrals, and rewrite the equation in form (11) in which we recognized the gradient sought $\nabla_z E$ (18). In the following we provide the explicit forms of $\partial u(r)/\partial \tau$ and $\nabla_z E$ for different choices of the radiative function. To obtain specific formulas we substitute $\mathcal{R} = 1$, $\mathcal{R} = (\mathbf{e}_r \cdot \mathbf{N})$, or $\mathcal{R} = (\mathbf{e}_r \cdot \mathbf{N})^2$ in equation (15) and we leverage the following mathematical relations:

$$(\mathbf{e}_r \cdot \mathbf{N}) = (\nabla r \cdot \mathbf{N}) = \frac{\frac{\partial r}{\partial z} - \frac{\partial z}{\partial x}\frac{\partial r}{\partial x} - \frac{\partial z}{\partial y}\frac{\partial r}{\partial y}}{\|J\|}, \tag{A.1}$$

$$2H = \frac{\left(1 + \left(\frac{\partial z}{\partial x}\right)^2\right)\frac{\partial^2 z}{\partial y^2} - 2\frac{\partial z}{\partial x}\frac{\partial z}{\partial y}\frac{\partial^2 z}{\partial x \partial y} + \left(1 + \left(\frac{\partial z}{\partial y}\right)^2\right)\frac{\partial^2 z}{\partial x^2}}{\|J\|^3}, \tag{A.2}$$

$$\nabla G \cdot \mathbf{N} = -\frac{\frac{\partial G}{\partial x}\frac{\partial z}{\partial x} + \frac{\partial G}{\partial y}\frac{\partial z}{\partial y}}{\|J\|}, \tag{A.3}$$

$$\nabla G \cdot \nabla r = \frac{\partial G}{\partial x}\frac{\partial r}{\partial x} + \frac{\partial G}{\partial y}\frac{\partial r}{\partial y}, \tag{A.4}$$

Radar-Based Reconstruction Using Variational Methods   26

some of which are specific to our choice of describing the surface as a graph of a function, with normal vector oriented upward. We recall that boundary terms in (15) will vanish by selecting an averaging window w fading to zero at its edges. Finally, in order to simplify the notation, let's consider just one antenna and drop index a.

Appendix A.1. Exploding reflector $\mathcal{R} = 1$

$$\frac{\partial u(r)}{\partial \tau} = \frac{1}{\Delta T} \int_{\mathcal{S} \cap \mathcal{Q}} \mathcal{V} \left[\frac{w}{r^4} \left(\nabla G \cdot \mathbf{N} \right) + \left(\frac{G}{r^4} \frac{\partial w}{\partial r} - \frac{4Gw}{r^5} \right) \left(\nabla r \cdot \mathbf{N} \right) - \frac{Gw}{r^4} 2H \right] \frac{\partial z}{\partial \tau} \, dx \, dy \ (A.5)$$

$$\nabla_z E = \frac{1}{\Delta T} \sum_{a=1}^{A} \int_{t_{min}}^{t_{max}} \chi_{\mathcal{Q}} \mathcal{V} \left(u_a(t) - u_a^0(t) \right) \left[\frac{w}{r^4} \left(\nabla G \cdot \mathbf{N} \right) \right.$$
$$\left. + \left(\frac{G}{r^4} \frac{\partial w}{\partial r} - \frac{4Gw}{r^5} \right) \left(\nabla r \cdot \mathbf{N} \right) - \frac{Gw}{r^4} 2H \right] dt \bigg|_{\mathbf{x}}$$
$$- \alpha_1 \triangle z \tag{A.6}$$

Appendix A.2. Cosine $\mathcal{R} = (\mathbf{e}_r \cdot \mathbf{N})$

$$\frac{\partial u(r)}{\partial \tau} = \frac{1}{\Delta T} \int_{\mathcal{S} \cap \mathcal{Q}} \mathcal{V} \left[\frac{G}{r^4} \frac{\partial w}{\partial r} + \frac{Gw}{r^4} \left(\nabla G \cdot \nabla r \right) - 2 \frac{Gw}{r^5} \right] \frac{\partial z}{\partial \tau} \, dx \, dy \tag{A.7}$$

$$\nabla_z E = \frac{1}{\Delta T} \sum_{a=1}^{A} \int_{t_{min}}^{t_{max}} \chi_{\mathcal{Q}} \mathcal{V} \left(u_a(t) - u_a^0(t) \right) \left[\frac{G}{r^4} \frac{\partial w}{\partial r} + \frac{Gw}{r^4} \left(\nabla G \cdot \nabla r \right) - 2 \frac{Gw}{r^5} \right] dt \bigg|_{\mathbf{x}} \tag{A.8}$$
$$- \alpha_1 \triangle z$$

Appendix A.3. Lambertian, $\mathcal{R} = (\mathbf{e}_r \cdot \mathbf{N})^2$, $\mathcal{H} = (\mathbf{e}_r \cdot \mathbf{N})$

$$\frac{\partial u(r)}{\partial \tau} = \frac{1}{\Delta T} \int_{\mathcal{S} \cap \mathcal{Q}} \mathcal{V} \left[-6 \frac{Gw}{r^5} \mathcal{H} + 2 \frac{G}{r^4} \frac{\partial w}{\partial r} \mathcal{H} + 2 \frac{Gw}{r^5} \| J \| \mathcal{R} \right.$$
$$- \frac{w}{r^4} \mathcal{R} \left(\nabla G \cdot \mathbf{N} \right) - \frac{G}{r^4} \frac{\partial w}{\partial r} \mathcal{R} \left(\nabla r \cdot \mathbf{N} \right) + \frac{4Gw}{r^5} \mathcal{R} \left(\nabla r \cdot \mathbf{N} \right)$$
$$+ \frac{Gw}{r^4} \mathcal{R} \left(2H \right) + 2 \mathcal{H} \frac{w}{r^4} \left(\nabla G \cdot \nabla r \right)$$
$$- 2 \frac{Gw}{r^4} \mathcal{H} \left(\frac{\frac{\partial r}{\partial x} \left(\frac{\partial z}{\partial x} \frac{\partial^2 z}{\partial x^2} + \frac{\partial z}{\partial y} \frac{\partial^2 z}{\partial y \partial x} \right) + \frac{\partial r}{\partial y} \left(\frac{\partial z}{\partial x} \frac{\partial^2 z}{\partial x \partial y} + \frac{\partial z}{\partial y} \frac{\partial^2 z}{\partial y^2} \right)}{\| J \|^2} \right)$$
$$\left. - 2 \frac{Gw}{r^4} \left(\frac{\frac{\partial^2 z}{\partial x^2} \left(\frac{\partial r}{\partial x} \right)^2 + 2 \frac{\partial^2 z}{\partial y \partial x} \frac{\partial r}{\partial x} \frac{\partial r}{\partial y} + \frac{\partial^2 z}{\partial y^2} \left(\frac{\partial r}{\partial y} \right)^2}{\| J \|} \right) \right] \frac{\partial z}{\partial \tau} \, dx \, dy \tag{A.9}$$

Radar-Based Reconstruction Using Variational Methods 27

$$
\begin{aligned}
\nabla_z E = {} & \frac{1}{\Delta T} \sum_{a=1}^{A} \int_{t_{min}}^{t_{max}} \chi_{\mathcal{Q}} \mathcal{V} \left(u_a(t) - u_a^0(t) \right) \left[-6 \frac{Gw}{r^5} \mathcal{H} + 2 \frac{G}{r^4} \frac{\partial w}{\partial r} \mathcal{H} \right. \\
& + 2 \frac{Gw}{r^5} \|J\| \, \mathcal{R} - \frac{w}{r^4} \mathcal{R} \left(\nabla G \cdot \mathbf{N} \right) - \frac{G}{r^4} \frac{\partial w}{\partial r} \mathcal{R} \left(\nabla r \cdot \mathbf{N} \right) \\
& + \frac{4Gw}{r^5} \mathcal{R} \left(\nabla r \cdot \mathbf{N} \right) + \frac{Gw}{r^4} \mathcal{R} \left(2H \right) + 2 \mathcal{H} \frac{w}{r^4} \left(\nabla G \cdot \nabla r \right) \\
& - 2 \frac{Gw}{r^4} \mathcal{H} \left(\frac{\frac{\partial r}{\partial x} \left(\frac{\partial z}{\partial x} \frac{\partial^2 z}{\partial x^2} + \frac{\partial z}{\partial y} \frac{\partial^2 z}{\partial y \partial x} \right) + \frac{\partial r}{\partial y} \left(\frac{\partial z}{\partial x} \frac{\partial^2 z}{\partial x \partial y} + \frac{\partial z}{\partial y} \frac{\partial^2 z}{\partial y^2} \right)}{\|J\|^2} \right) \\
& \left. - 2 \frac{Gw}{r^4} \left(\frac{\frac{\partial^2 z}{\partial x^2} \left(\frac{\partial r}{\partial x} \right)^2 + 2 \frac{\partial^2 z}{\partial y \partial x} \frac{\partial r}{\partial x} \frac{\partial r}{\partial y} + \frac{\partial^2 z}{\partial y^2} \left(\frac{\partial r}{\partial y} \right)^2}{\|J\|} \right) \right] dt \Bigg|_{\mathbf{x}} \\
& - \alpha_1 \triangle z
\end{aligned}
\tag{A.10}
$$

Appendix B. Algorithms for the direct computation of Reflectivity

Appendix B.1. Piecewise reflectivity

Assuming we are considering finite time intervals $t_m = t_{min} + m \, \Delta t$. For each antenna - time window pair (a, t_m) we demand $(u_a(t_m) - u_a^0(t_m)) = 0$. Assuming that it exist a constant value of G_{am} on the portion of surface individuated by the (a, t_m) combination, we rewrite the latter equation using (13)

$$
u_a(t_m) = G_{am} \frac{1}{\Delta t} \left(\int_{\mathcal{S} \cap \mathcal{Q}} \mathcal{V} \frac{w \mathcal{R}}{r^4} \|J\| \, dx \, dy \right) = G_{am} \hat{W}_{am}
\tag{B.1}
$$

we obtain

$$
G_{am} = \frac{u_{am}^0}{\hat{W}_{am}}
\tag{B.2}
$$

therefore a value of "apparent" G is obtained. Considering now a point p on the surface, located at position $\mathbf{x}$ with an associated infinitesimal area da (that in the practical computation it will be associated to a node of the computational grid), we know from the forward model equations that the point contributes to a specific (a, t_m) pair, in which it is included, as

$$
\begin{aligned}
C_{am} &= G(\mathbf{x}) \mathcal{V} \frac{w \mathcal{R}}{r^4} da \\
&= G(\mathbf{x}) H_{am} .
\end{aligned}
\tag{B.3}
$$

Actually, point p will most probably contribute to several time windows for the same antenna a, and to several antennas. As such, we expect that it will contribute in the computation of several $u_a(t_m)$ and in turn, to several G_{am}. Therefore, in order to estimate $G(\mathbf{x})$ from this set of apparent values we use a weighted average.

$$
G(\mathbf{x}) = \frac{\sum_a^A \sum_m^M G_{am} H_{am}}{\sum_a^A \sum_m^M H_{am}}
\tag{B.4}
$$

Radar-Based Reconstruction Using Variational Methods   28

Appendix B.2. Constant reflectivity

Starting from equation (9), we consider the partial derivative of the energy with respect to G:

$$\frac{\partial E}{\partial G} = \sum_{a=1}^{n_a} \int_{t_{min}}^{t_{max}} \left(u_a(t) - u_a^0(t) \right) \frac{\partial u_a(t)}{\partial G} \, dt \tag{B.5}$$

imposing this equation to be zero,

$$\sum_{a=1}^{A} \int_{t_{min}}^{t_{max}} \left(u_a(t) - u_a^0(t) \right) \frac{\partial u_a(t)}{\partial G} \, dt = 0 \tag{B.6}$$

$$\sum_{a=1}^{A} \int_{t_{min}}^{t_{max}} u_a(t) \frac{\partial u_a(t)}{\partial G} \, dt = \sum_{a=1}^{A} \int_{t_{min}}^{t_{max}} u_a^0(t) \frac{\partial u_a(t)}{\partial G} \, dt \tag{B.7}$$

then computing $\partial u_a(t) / \partial G$, and assuming G is constant across the surface

$$u_a(t) = G \frac{1}{\Delta t} \left(\int_{\mathcal{S} \cap \mathcal{Q}} \mathcal{V} \frac{w \mathcal{R}}{r^4} \, \|J\| \, dx \, dy \right) = G \hat{W}_a(t) \tag{B.8}$$

$$\frac{\partial u_a(t)}{\partial G} = \frac{1}{\Delta t} \left(\int_{\mathcal{S} \cap \mathcal{Q}} \mathcal{V} \frac{w \mathcal{R}}{r^4} \, \|J\| \, dx \, dy \right) = \hat{W}_a(t) \tag{B.9}$$

note that $\hat{W}_a(t)$ is independent of G, therefore

$$\sum_{a=1}^{A} \int_{t_{min}}^{t_{max}} u_a(t) \frac{\partial u_a(t)}{\partial G} \, dt = \sum_{a=1}^{A} \int_{t_{min}}^{t_{max}} u_a^0(t) \frac{\partial u_a(t)}{\partial G} \, dt \tag{B.10}$$

$$G \sum_{a=1}^{A} \int_{t_{min}}^{t_{max}} \hat{W}_a(t) \, \hat{W}_a(t) \, dt = \sum_{a=1}^{A} \int_{t_{min}}^{t_{max}} u_a^0(t) \, \hat{W}_a(t) \, dt \tag{B.11}$$

$$\tag{B.12}$$

finally

$$G = \frac{\sum_{a=1}^{A} \int_{t_{min}}^{t_{max}} u_a^0(t) \, \hat{W}_a(t) \, dt}{\sum_{a=1}^{A} \int_{t_{min}}^{t_{max}} \hat{W}_a^2(t) \, dt} \tag{B.13}$$

References

Bagheri, H., Schmitt, M., d'Angelo, P. & Zhu, X. X. (2018). A framework for sar-optical stereogrammetry over urban areas, *ISPRS journal of photogrammetry and remote sensing* **146**: 389–408.

Bamler, R. & Hartl, P. (1998). Synthetic aperture radar interferometry, *Inverse Problems* **14**(4): R1–R54.

Barnes, C. F. (2015). *Synthetic Aperture Radar: Wave Theory Foundations, Analysis and Algorithms*, first edn, Barnes, Powder Springs, Georgia.

Barnes, C. F. & Prasad, S. (2018). In situ volumetric SAR, *IEEE Transactions on Geoscience and Remote Sensing* **56**(10): 6082–6100.

Bertero, M. & Piana, M. (2006). Inverse problems in biomedical imaging: modeling and methods of solution, *in* V. A. Quarteroni A., Formaggia L. (ed.), *Complex Systems in Biomedicine*, Springer, Milano, pp. 1–33.

Bignardi, S., Fedele, F., Yezzi, A., Rix, G. J. & Santarato, G. (2012). Geometric seismic-wave inversion by the boundary element method, *Bulletin of the Seismological Society of America* **102**: 802–811.

Brozovic, M., Ostro, S. J., Benner, L., Giorgini, J. D., Jurgens, R. F., Rose, R., Nolan, M. C., Hine, A. A., Magri, C., Scheeres, D. J. & Margot, J. (2009). Radar observations and a physical model of asteroid 4660 nereus, a prime space mission target, *Icarus* **201**: 153–166.

Carrara, W. G., Goodman, R. S. & Majewski, R. M. (1995). *Spotlight Synthetic Aperture Radar: Signal Processing Algorithms*, Artech House, Boston, Massachusetts.

Cheng, P., Steen, G., Yezzi, A. & Krim, H. (2009). Brain MRI T1-map and T1-weighted image segmentation in a variational framework, *IEEE International Conference on Acoustics Speech and Signal Processing*, pp. 417–420.

Cloude, S. R. (2010). *Polarisation: Applications in Remote Sensing*, Oxford University Press Inc., New York.

Comelli, A., Bignardi, S., Stefano, A., Russo, G., Sabini, M. G., Ippolito, M. & Yezzi, A. (2020). Development of a new fully three-dimensional methodology for tumours delineation in functional images, *Computers in Biology and Medicine* **120**: 103701.

Cook, D. A., Mueller, M. F., Fedele, F. & Yezzi, A. (2014). Adjoint active surfaces for localization and imaging, *IEEE Transactions on Image Processing* **24**: 316–331.

Cosentino, P. L., Capizzi, P., Martorana, R., Messina, P. & Schiavone, S. (2011). From geophysics to microgeophysics for engineering and cultural heritage, *International Journal of Geophysics* .

Curlander, J. C. & McDonough, R. N. (1991). *Synthetic Aperture Radar: Systems and Signal Processing*, John Wiley & Sons, New York.

Das, Y. & Boerner, W. M. (1978). On radar target shape estimation using algorithms for reconstruction from projections, *IEEE Transactions on Antennas and Propagation* **AP-26**(2): 274–279.

Deepak., A. (1977). *Inversion Methods in Atmospheric Remote Sounding*, Elsevier.

Farhat, N. H. (1975). High resolution microwave holography and the imaging of remote objects, *Optical Engineering* **14**(5): 499–505.

Gallego, G., Yezzi, A., Fedele, F. & Benetazzo, A. (2011). A variational stereo method for the three-dimensional reconstruction of ocean waves, *IEEE Transactions on Geoscience and Remote Sensing* **49**(11): 4445–4457.

Gonzalez-Valdes, B., Martinez-Lorenzo, J. A. & Rappaport, C. M. (2013). A new fast algorithm for radar-based shape reconstruction of smoothly varying objects, *IEEE Antennas and Wireless Propagation Letters* **12**: 484–487.

Groetsch, C. W. (1984). *The theory of Tikhonov regularization for Fredholm integral equations of the first kind*, Pitman Publishing Inc., Marshfield, Massachusetts, USA.

Hailin, J., Yezzi, A. J. & Soatto, S. (2002). Variational multiframe stereo in the presence of specular reflections, *Proceedings. First International Symposium on 3D Data Processing Visualization and Transmission*, Padova, Italy, pp. 626–630.

Hamasaki, T.and Sato, M., Ferro-Famil, L. & Pottier, E. (2005). Polarimetric sar stereo using pi-sar square loop path, *Proceedings. 2005 IEEE International Geoscience and Remote Sensing Symposium, 2005. IGARSS '05.*, Vol. 1, p. 4 pp.

Haukas, J., Ravndal, O., Fotland, B. H., Bounaim, A. & Sonneland, L. (2013). Automated salt body extraction from seismic data using level set method, *First Break* **31**: 35–42.

Herman, R. (2001). An introduction to electrical resistivity in geophysics, processing and interpretation, *American Journal of Physics* **69**: 943–952.

Hounsfield, G. N. (1973). Computerized transverse axial scanning tomography. part i: Description of the system, *British Journal of Radiology* **46**: 1016–1022.

Hudson, S. (1993). Three-dimensional reconstruction of asteroids from radar observations, *Remote Sensing Reviews* **8**: 195–203.

Jin, H., Yezzi, A., Tsai, Y., Cheng, L. & Soatto, S. (2003). Estimation of 3D surface shape and smooth radiance from 2D images: A level set approach, *Journal of Scientific Computing* **19**: 267–292.

Kichenassamy, S., Kumar, A., Olver, P., Tannenbaum, A. & Yezzi, A. (1995). Gradient flows and

Radar-Based Reconstruction Using Variational Methods 30

geometric active contour models, *Proceedings of IEEE International Conference on Computer Vision*, pp. 810–815.

Koyama, C. N., Gokon, H., Jimbo, M., Koshimura, S. & Sato, M. (2016). Disaster debris estimation using high-resolution polarimetric stereo-sar, *ISPRS Journal of Photogrammetry and Remote Sensing* **120**: 84–98.

Loke, M. & Barker, R. (1996). Practical techniques for 3D resistivity surveys and data inversion, *Geophysical prospecting* **44**(3): 499–523.

Louie, J. N. (2001). Faster, better: Shear-wave velocity to 100 meters depth from refraction microtremor arrays, *Bulletin of the Seismological Society of America* **91**(2): 347–364.

Munson, Jr, D. C. (1987). An introduction to strip-mapping synthetic aperture radar, *Proceedings of the IEEE International Conference on Acoustics, Speech, and Signal Processing*, Dallas, Texas, pp. 2245–2248.

Oliver, C. J. (1989). Synthetic-aperture radar imaging, *Journal of Physics D: Applied Physics* **22**(7): 871–890.

Park, C. B., D., M. R. & Xia, J. (1999). Multichannel analysis of surface waves, *Geophysics* **64**: 800–808.

Raknes, E. & Arntsen, B. (2014). Time-lapse full-waveform inversion of limited-offset seismic data using a local migration regularization, *Geophysics* **79**(3): WA117–WA128.

Sambuelli, L., Bohm, G., Capizzi, P., Cardarelli, E. & Cosentino, P. (2011). Comparison between gpr measurements and ultrasonic tomography with different inversion algorithms: an application to the base of an ancient egyptian sculpture, *Journal of Geophysics and Engineering* **8**(3): S106–S116.

Shafiq, M., Wang, Z. & Alregib, G. (2015). Seismic interpretation of migrated data using edge-based geodesic active contours, *Proceedings of the IEEE Global Conference on Signal and Information Processing*, Orlando, Florida, USA.

Soumekh, M. (1999). *Synthetic Aperture Radar Signal Processing with MATLAB Algorithms*, John Wiley & Sons.

Tarantola, A. (2005). *Inverse Problem Theory and Model Parameter Estimation*, SIAM, Philadelphia, Pennsylvania, USA.

Thomas, J., Kober, W. & Leberl, F. (1989). Multiple-image sar shape from shading, *Remote Sensing, an economic tool for the nineties*, Vol. 2, New York, NY: Institute of Electrical and Electronics Engineers, pp. 592–596.

Virieux, J. & Operto, S. (2009). An overview of full-waveform inversion in exploration geophysics, *Geophysics* **74**(6): 127–152.

Walker, J. L. (1980). Range-Doppler imaging of rotating objects, *IEEE Transactions on Aerospace and Electronic Systems* **16**(1): 23–52.

Yezzi, A., Kichenassamy, S., Kumar, A., Olver, P. & Tannenbaum, A. (1997). A geometric snake model for segmentation of medical imagery, *IEEE Transactions on medical imaging* **16**(2): 199–209.

Yezzi, A. & Soatto, S. (2003). Stereoscopic segmentation, *International Journal of Computer Vision* **53**: 31–43.

Yildirim, A. (2019). *A Geometrical Variational Approach to Shape Inversion for Radar*, PhD thesis, Georgia Institute of Technology.

Yildirim, A. & Yezzi, A. (2018). Developing a geometric deformable model for radar shape inversion, *Proceedings of the ICASSP, IEEE International Conference on Acoustics, Speech and Signal Processing*, Vol. Article number 8461926, April 15-20, Calgary, Canada, pp. 6483–6487.

Yildirim, A., Yezzi, A., Bignardi, S. & Barnes, C. F. (2020). A geometric approach to radar based 2d shape inversion.